

# MagDot: Drift-free, Wearable Joint Angle Tracking at Low Cost

DONGYAO CHEN, Shanghai Jiao Tong University

QING LUO, Shanghai Jiao Tong University

XIAOMENG CHEN, Shanghai Jiao Tong University

XINBING WANG, Shanghai Jiao Tong University

CHENGHU ZHOU, Chinese Academy of Sciences

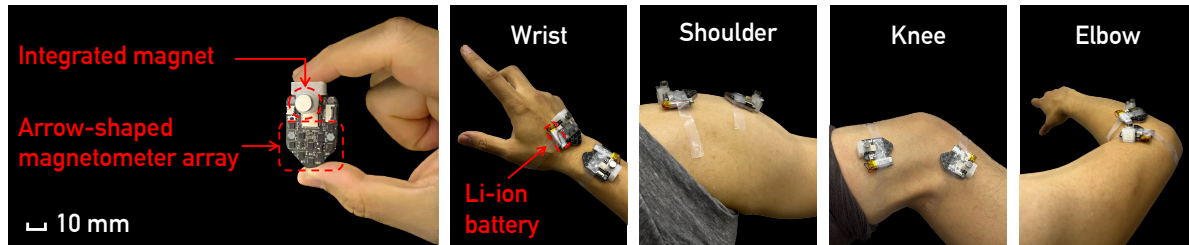


Fig. 1. MagDot sensing unit and its applicability. MagDot units can be attached to different types of joints, e.g., wrist, shoulder, knee, and elbow. By sensing the relative position between two units, MagDot system can accurately measure joint angles.

Tracking the angular movement of body joints has been a critical enabler for various applications, such as virtual and augmented reality, sports monitoring, and medical rehabilitation. Despite the strong demand for accurate joint tracking, existing techniques, such as cameras, IMUs, and flex sensors, suffer from major limitations that include occlusion, cumulative error, and high cost. These issues collectively undermine the practicality of joint tracking.

We introduce MagDot, a new magnetic-based joint tracking method that enables high-accuracy, drift-free, and wearable joint angle tracking. To overcome the limitations of existing techniques, MagDot employs a novel tracking scheme that compensates for various real-world impacts, achieving high tracking accuracy. We tested MagDot on eight participants with a professional motion capture system, i.e., Qualisys motion capture system with nine Arqus A12 cameras. The results indicate MagDot can accurately track major body joints. For example, MagDot can achieve tracking accuracy of  $2.72^\circ$ ,  $4.14^\circ$ , and  $4.61^\circ$  for elbow, knee, and shoulder, respectively. With a power consumption of only  $98\text{ mW}$ , MagDot can support one-day usage with a small battery pack.

CCS Concepts: • **Hardware** → *Sensor devices and platforms*.

Additional Key Words and Phrases: Magnetic Sensing, Joint Angle, Motion Capture

Authors' addresses: Dongyao Chen, chendy@sjtu.edu.cn, Shanghai Jiao Tong University; Qing Luo, luqing@sjtu.edu.cn, Shanghai Jiao Tong University; Xiaomeng Chen, sjtu\_chenxm@sjtu.edu.cn, Shanghai Jiao Tong University; Xinbing Wang, xwang8@sjtu.edu.cn, Shanghai Jiao Tong University; Chenghu Zhou, zhouch@lreis.ac.cn, Chinese Academy of Sciences.

Permission to make digital or hard copies of all or part of this work for personal or classroom use is granted without fee provided that copies are not made or distributed for profit or commercial advantage and that copies bear this notice and the full citation on the first page. Copyrights for components of this work owned by others than the author(s) must be honored. Abstracting with credit is permitted. To copy otherwise, or republish, to post on servers or to redistribute to lists, requires prior specific permission and/or a fee. Request permissions from [permissions@acm.org](mailto:permissions@acm.org).

© 2023 Copyright held by the owner/author(s). Publication rights licensed to ACM.

2474-9567/2023/12-ART150 \$15.00

<https://doi.org/10.1145/3631423>

## 1 INTRODUCTION

Accurate measurement of joint angles is vital for various interdisciplinary applications, including medical care [19, 34, 42], sports analytics [50, 54, 61], and computer-human interaction [44, 49]. For example, monitoring the shoulder joint angle accurately and continuously is pivotal in rehabilitating common diseases such as frozen shoulder [25]. Tracking joint angles during athletic performance can help coaches and athletes analyze and enhance their techniques. Furthermore, precise and robust joint angle measurements can improve human-computer interaction and create more immersive experiences in the realm of virtual and augmented reality.

Over the past decade, the increasing demand for practical joint tracking has prompted the development of several innovative methods. Inertial measurement units (IMUs) leverage gyroscope data to determine angular information, while camera-based techniques rely on computer vision to process image data. Recently, researchers have explored conductive stretchable material to build flex sensors [23, 29, 36] for joint tracking. Despite these advancements, existing methods often face the following limitations that hinder their practicality.

**Error-prone.** Existing joint angle tracking methods face challenges in achieving high tracking precision. For example, IMU-based methods suffer from accumulative errors over time when integrating motion sensor readings to derive joint angles. Even top-grade IMU sensors, such as XSens [16], exhibit fast-accumulating errors, with the angular error escalating from  $9.70^\circ$  to  $10.68^\circ$  within 30 seconds of usage, as observed in our empirical studies (Sec. 6). Camera-based methods often encounter occlusion issues in real-world scenarios, which disrupt the measurement process and lead to tracking inaccuracies. Similarly, other schemes like RF-based approaches (e.g., RFID, mmWave) are also susceptible to real-world interference, impacting their tracking performance. In Sec. 2 and Sec. 8, we analyze the root causes of these issues. In Sec. 5 and Sec. 6, we present the results of our empirical study, highlighting the limitations of current approaches for joint angle tracking.

**High cost.** Accurate joint angle tracking systems are often prohibitively expensive. For instance, the state-of-the-art IMU approach attaches sensing units to users' bodies to derive angular information. However, the cost of high-precision IMUs can be exorbitant, with the basic-level tracking set costing more than \$4,500 (approx. \$260 per unit). Vision-based Qualisys and Vicon motion capture (mocap) systems [11, 14] are considered the "gold standard" for joint angle analysis. These systems require multiple pre-installed cameras in a spacious testing area and reflective on-body markers. The cost of a complete tracking set can exceed \$180,000, with individual cameras priced at around \$20,000 each.

This paper presents MagDot, a wearable system that uses magnetic sensing to track the joint angle with high precision. With its novel design, MagDot provides *robust, drift-free* performance at a fraction of the cost of existing methods. As we elaborate in Sec. 4, each unit costs less than \$35.

MagDot uses magnetic sensing to achieve joint tracking. Magnetic sensing uses magnetometers to sense the nearby magnetic field. For example, one can use a compact magnetometer array to derive the 3D position of the targeted passive magnet [21, 60]. Although magnetic sensing is immune to accumulative error, it suffers from a wide range of real-world impacts, thus severely undermining its performance. In this work, we tackle *three* key challenges to make MagDot practical for real-world joint tracking applications.

**1. Wearable form factor for joint tracking.** To achieve accurate and reliable joint angle tracking, a wearable joint tracking system should be able to accommodate different joint moving patterns and geometries. Joints have varying degrees of freedom (DoF), with 1-DoF joints such as elbow and knee and 2-DoF joints such as shoulder, wrist, and hip. Additionally, factors such as height and body weight can lead to different joint sizes. To address these challenges, we propose a novel tracking platform design with a compact size and an *integrated magnet* that can support both 1-DoF and 2-DoF joint tracking. As shown in Fig. 1, our design features a miniature form factor of  $2.5\text{ cm} \times 1.3\text{ cm} \times 2.1\text{ cm}$ , which incurs minimal burden for the user and improves the overall user experience. This design enables versatile usage of tracking different types of joint by attaching two MagDot units on the joint. We will articulate our algorithm and hardware design in Sec. 3 and Sec. 4, respectively.



**2. Temperature compensation.** MEMS magnetometers are highly sensitive to changes in temperature, which can result in significant variations in sensor readings. As discussed in Sec. 3, these temperature changes can cause abrupt shifts in the readings, which can severely affect the accuracy of joint tracking applications. While existing guidelines have proposed methods for compensating for temperature drift, these approaches are typically coarse-grained and are not suitable for high-precision joint tracking applications. To address this issue, MagDot proposes a novel compensation scheme that can automatically derive the appropriate configuration for effective temperature compensation. With this design, we achieve high-performance joint tracking with commodity-off-the-shelf (COTS) Hall effect magnetometers, ensuring the tracking performance is robust in varying settings.

**3. Skin deformation.** The MagDot joint tracking system is designed to overcome significant obstacles in wearable joint tracking. One major challenge is skin deformation, leading to misalignment between the sensor and bone coordinates when a joint moves due to muscle movement. To address this issue, MagDot employs a one-time configuration compensation method, which is discussed in detail in Sec. 3. This configuration is also resilient to repositioning errors, as demonstrated in our evaluation in Sec. 6, where the experiment subjects take off and put back the sensing module without affecting the tracking accuracy. By overcoming the skin deformation problem, MagDot enhances its accuracy and robustness in practical applications.

To assess MagDot's performance, we conducted a two-stage evaluation of MagDot in real-world settings. In the first stage, we proposed a cost-efficient setup to evaluate the angular accuracy of MagDot. Specifically, we used 3D-printed joint models to examine the performance. This experiment setup helps us iterate the design of MagDot without the need for expensive mocap gears. In the second stage, we performed on-body experiments with the high-precision, full-fledged mocap system, i.e., nine Qualisys Arqus A12 cameras and reflective on-body markers. Our empirical studies indicate MagDot can achieve a high tracking accuracy of  $2.72^\circ$  and  $4.61^\circ$  angular errors for 1-DoF and 2-DoF joints, respectively. We also compared MagDot's performance with high-end IMUs in varying activities. Specifically, for walking, jogging, and running motions, MagDot can track the knee angle at errors of  $4.14^\circ$ ,  $4.88^\circ$ , and  $6.32^\circ$ , respectively. In contrast, the state-of-the-art IMU method exhibits tracking errors of  $5.71^\circ$ ,  $7.53^\circ$ , and  $10.27^\circ$  for the same activity set. As we will elaborate in Sec. 6, IMU also shows accumulating drift error for the same motion. MagDot incurs a low energy overhead at only  $98\text{ mW}$ , which is sufficient to enable *one-day usage* with a small  $220\text{ mAh}$  battery pack. As we will elaborate in the empirical study, compared with IMU-based method, MagDot achieves superior tracking accuracy with similar wearability. Specifically, one needs to attach two MagDot units on both the distal and proximal segments of the targeted joint. IMU-based method also requires the user to wear two units on both the distal and proximal segments for deriving the joint angle. Compared with IMU sensors, which derive the absolute attitude, MagDot is more privacy-preserving as it only tracks the angle of the joint.

This paper has the following contributions: (1) Introducing MagDot, a compact, fully wearable joint measurement system that uses a novel magnetic sensing platform. MagDot provides precise joint angle measurements that are drift-free and adaptable to various joint types. (2) Addressing various real-world interferences, making MagDot a practical solution for continuous joint tracking. (3) Conducting comprehensive real-world experiments, demonstrating the feasibility of MagDot for various applications.

## 2 BACKGROUND AND MOTIVATION

### 2.1 Structure of Body Joints

In this paper, we focus on two major movement patterns of body joints. As shown in Fig. 2 (a), 1-DoF joints enable a single angular movement, specifically flexion and extension motions. 1-DoF joints can denote hinge joints — a major category of body joints including knee and elbow. 2-DoF joints enable more diverse body movement. Specifically, 2-DoF joints can represent ball-and-socket joints (e.g., shoulder and hip) and condyloid joints (e.g., wrist) [18]. For example, in a ball-and-socket joint, the distal bone usually has a ball-shaped tip, which can fit

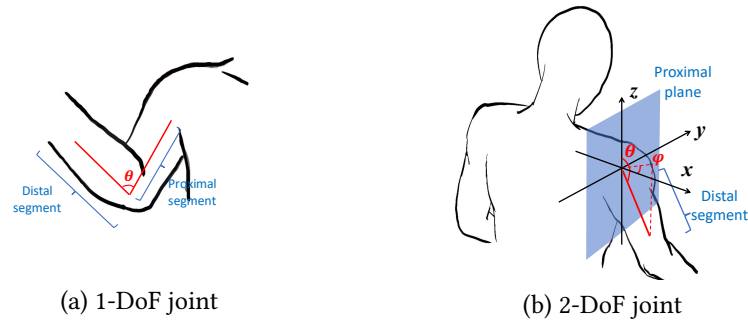


Fig. 2. Exemplary joint models, e.g., elbow and shoulder joints.

into the socket on the proximal bone. The axis of the distal bone can move in an indefinite number of directions, centers at the socket. As a result, one can use two angular changes, i.e.,  $\theta$  and  $\phi$  as shown in Fig. 2 (b), to denote the 2-DoF movement.

## 2.2 IMU-based Sensing Techniques

IMUs use motion sensors, such as a gyroscope and an accelerometer, and may also have an embedded magnetometer. IMUs are immune to occlusion, a major limitation of vision-based methods.

Now, we articulate the major limitation of IMUs for tracking joint angles. To determine the joint angle, IMU *integrates* the angular velocity data obtained from the gyroscope to derive the required 3D rotation of its ego coordinate. However, the raw data from the gyroscope contains noise, which can be amplified during the integration process, leading to rapid drift in the angular data. This drift can significantly impair the accuracy of joint angle measurement over time.

Additional direction references, such as gravity and magnetic poles, are commonly used to address the drift problem in IMU data. Legacy algorithms, such as the Madgwick [38] and Mahony [39] algorithms, assume that the direction of the accelerometer is aligned with the local gravity. Similarly, the magnetometer reading is assumed to be aligned with the local Earth magnetic field. By combining this estimation from gravity and magnetic poles with gyroscope data, one can obtain the 3D orientation of the IMU. Recent progresses in IMU-based methods, e.g.,  $A^3$  [71] and *Muse* [53], selectively use these references to achieve higher accuracy. That is, state-of-the-art IMU schemes still rely closely on gravity and magnetic references.

Due to the above intrinsic limitations, IMU-based methods are *error-prone* for joint tracking tasks. The fusion algorithm used in IMU can only produce accurate results in static, demagnetized environments. When there is movement, the accelerometer measures the integration of gravity and linear motion, leading to inaccurate estimations of acceleration. Environmental magnetic interference can also pollute magnetometer readings, making it challenging to determine the magnetic direction. As a result, both references become unreliable, causing drifts in the derived joint angles. We provide empirical study results in Sec. 5 and Sec. 6 to support these assessments.

## 2.3 Why Magnetic Sensing?

Passive magnets and magnetometers are emerging as promising techniques for high-precision sensing. Recent efforts, such as [21], have leveraged magnetometer arrays to determine the position of nearby magnets accurately. As we will articulate in Sec. 3, magnetic sensing offers several benefits, including its drift-free nature and cost-effectiveness. Moreover, since it tracks the relative position between the sensor array and magnets, it is not affected by occlusion.

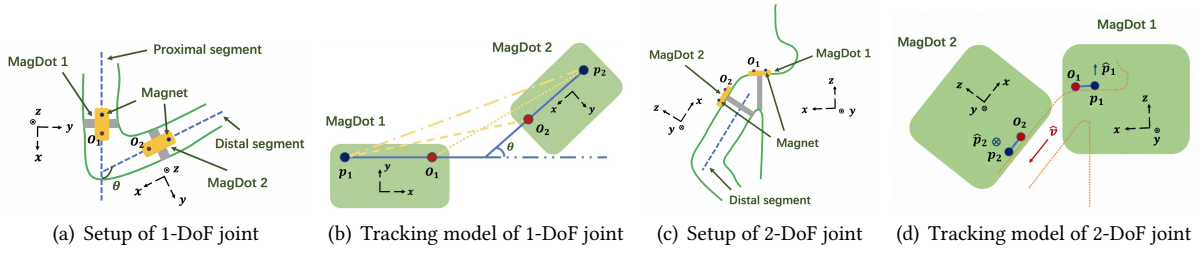


Fig. 3. Schematic of the 1-DoF and 2-DoF joint tracking approaches.

Despite these advantages, integrating magnetic sensing into joint angle tracking is challenging. Specifically, traditional magnetic sensing techniques rely on a single magnetic sensor array to track the position of permanent magnets. Therefore, to derive the relative pose between the distal and proximal segments, this method requires *precise measurements* of the distance between the magnet and the sensor array to the joint axis. This stringent requirement can be problematic for users. For example, displacement can occur when the user remounts the sensing module. As a result, the displacement of the sensor array and/or magnet can lead to significant deviations in joint tracking results.

Magnetometers may be susceptible to real-world disturbances. For example, MEMS (micro-electromechanical systems) magnetometers may be influenced by temperature variations. In the following sections of this paper, we will discuss the key designs of the MagDot system and address these challenges.

### 3 THE SENSING PRINCIPLES OF MAGDOT

We introduce a novel magnet-integrated sensing platform. Unlike conventional magnetic tracking layout, our novel platform uses two homogeneous MagDot units. *This design allows either MagDot unit to sense the magnet on another MagDot unit.* Specifically, 1) users do not need to measure the precise placement of the sensor module on joints; 2) the symmetrical design allows a compact form factor of MagDot, accommodating various joint types, as illustrated in Fig. 1. In Sec. 3.1 and Sec. 3.2, we will articulate the tracking algorithm for 1-DoF and 2-DoF joints, respectively. Sec. 3.3 presents MagDot's core magnetic tracking algorithm. To further enhance the robustness of MagDot, we tackle two major interferences, i.e., skin deformation and thermal drift, in Sec. 3.5 and Sec. 3.4. As we will elaborate in this section, our new thermal drift compensation is a one-time effort. The user only needs to perform a quick calibration of skin deformation to safeguard MagDot's tracking accuracy.

#### 3.1 Tracking Algorithm of the 1-DoF Joint

To track the angle of a 1-DoF joint, we place two MagDot units on distal and proximal segments, as shown in Fig. 3(a). The layout of MagDot units can be projected onto the x-y plane parallel to the joint angle as shown in Fig. 3(b). The coordinate systems of the two MagDot units are projected onto two new rectangular coordinate systems, labeled as  $S_1$  and  $S_2$ , respectively. In Fig. 3(b),  $p_1$  and  $p_2$  represent the positions of the integrated magnets on the two sensing units, respectively.  $O_1$  and  $O_2$  indicate the origins of the two coordinate systems. We denote the angle of the 1-DoF joint as  $\theta$ .

From the internal layout of MagDot units, we can determine the values of vector  $O_1p_1$  in  $S_1$  and vector  $O_2p_2$  in  $S_2$ , denoted as  $O_1p_1(S_1)$  and  $O_2p_2(S_2)$ , respectively. With the magnetic tracking method as we elaborated in Sec. 3.3, we can derive the values of vector  $O_1p_2$  in  $S_1$  and vector  $O_2p_1$  in  $S_2$ , denoted as  $O_1p_2(S_1)$  and  $O_2p_1(S_2)$ ,

respectively. Therefore, as shown below, we can derive the vector  $\mathbf{p}_1\mathbf{p}_2$  in  $S_1$  and  $S_2$ .

$$\begin{cases} \mathbf{p}_1\mathbf{p}_2(S_1) = \mathbf{O}_1\mathbf{p}_2(S_1) - \mathbf{O}_1\mathbf{p}_1(S_1) \\ \mathbf{p}_1\mathbf{p}_2(S_2) = \mathbf{O}_2\mathbf{p}_2(S_2) - \mathbf{O}_2\mathbf{p}_1(S_2) \end{cases} \quad (1)$$

We denote coordinates of  $\mathbf{p}_1\mathbf{p}_2(S_1)$  and  $\mathbf{p}_1\mathbf{p}_2(S_2)$  as  $(x_1, y_1)$  and  $(x_2, y_2)$ , respectively. From Fig. 3 (b), we can obtain the coordinate system  $S_2$  by counterclockwise rotating  $S_1$  in an angle of  $\theta + \pi$ , followed by a translation along the distance between  $O_1$  and  $O_2$ . Note that the translation transformation of a coordinate system does not alter its vectors. Therefore,  $\mathbf{p}_1\mathbf{p}_2(S_1)$  and  $\mathbf{p}_1\mathbf{p}_2(S_2)$  satisfy the following formula.

$$\begin{bmatrix} x_2 \\ y_2 \end{bmatrix} = \begin{bmatrix} \cos(\theta + \pi) & \sin(\theta + \pi) \\ -\sin(\theta + \pi) & \cos(\theta + \pi) \end{bmatrix} \begin{bmatrix} x_1 \\ y_1 \end{bmatrix} \quad (2)$$

Note that the calculation of  $x_1, y_1$  and  $x_2, y_2$  does not require measuring the distance from the two sensing units to the joint center. Therefore, this transition allows MagDot to track the angle *without* using the precise placement of each unit. This feature can effectively improve the usability of MagDot.

By solving the above equations, one can derive the presentation of  $\theta$  as:

$$\theta = \begin{cases} \arccos\left(\frac{x_1x_2 + y_1y_2}{x_1^2 + y_1^2}\right), & x_1y_2 \geq y_1x_2 \\ -\arccos\left(\frac{x_1x_2 + y_1y_2}{x_1^2 + y_1^2}\right), & x_1y_2 < y_1x_2 \end{cases} \quad (3)$$

Due to the possibility of tracking errors in the position of the magnets, it is important to note that the magnitudes of  $\mathbf{p}_1\mathbf{p}_2(S_1)$  and  $\mathbf{p}_1\mathbf{p}_2(S_2)$  may not be equal. This can result in erroneous joint angle calculations. To address this issue, it is necessary to normalize the magnitudes of  $\mathbf{p}_1\mathbf{p}_2(S_1)$  and  $\mathbf{p}_1\mathbf{p}_2(S_2)$  before using Eq. 3 to solve for the joint angle.

### 3.2 Tracking Algorithm of the 2-DoF Joint

To track the two joint angles of a 2-DoF joint, one sensing unit is attached to the limb rotating around the joint center (MagDot #2); the other unit should be attached to the torso or proximal limb (MagDot #1). This setup is illustrated in Fig. 3(c). A spatial Cartesian coordinate system is established for each MagDot unit, denoted as  $S_1$  and  $S_2$  for MagDot #1 and #2, respectively. The tracking model of MagDot units in the 2-DoF setting is depicted in Fig. 3(d). The coordinate origins of  $S_1$  and  $S_2$  are denoted as  $O_1$  and  $O_2$ , respectively.  $p_1$  and  $p_2$  represent the positions of the two magnets, with orientations  $\hat{\mathbf{p}}_1$  and  $\hat{\mathbf{p}}_2$ . The direction vector of the limb rotating around the joint center is denoted as  $\hat{\mathbf{v}}$ .

The joint angles (as shown in Fig. 2) of the 2-DoF joint are determined as follows:  $\theta$  is the angle between  $\hat{\mathbf{v}}$  and the z-axis of  $S_1$ ;  $\phi$  is the angle between the projection of  $\hat{\mathbf{v}}$  onto the x-y plane of  $S_1$  and the x-axis.

Compared with the tracking algorithm of 1-DoF joint, the 2-DoF joint tracking model requires not only the position vectors of magnets but also the orientation vectors. Specifically, based on the layout of the sensor array and its corresponding magnet, we can determine  $\mathbf{O}_1\mathbf{p}_1(S_1)$ ,  $\hat{\mathbf{p}}_1(S_1)$ ,  $\mathbf{O}_2\mathbf{p}_2(S_2)$ ,  $\hat{\mathbf{p}}_2(S_2)$ , and  $\hat{\mathbf{v}}(S_2)$ . With the magnetic tracking method, we can derive the values of  $\mathbf{O}_1\mathbf{p}_2(S_1)$ ,  $\mathbf{O}_2\mathbf{p}_1(S_2)$ ,  $\hat{\mathbf{p}}_1(S_2)$  and  $\hat{\mathbf{p}}_2(S_1)$ . Then we can denote  $\mathbf{p}_1\mathbf{p}_2$  in  $S_1$  and  $S_2$  as follows:

$$\begin{cases} \mathbf{p}_1\mathbf{p}_2(S_1) = \mathbf{O}_1\mathbf{p}_2(S_1) - \mathbf{O}_1\mathbf{p}_1(S_1) \\ \mathbf{p}_1\mathbf{p}_2(S_2) = \mathbf{O}_2\mathbf{p}_2(S_2) - \mathbf{O}_2\mathbf{p}_1(S_2) \end{cases} \quad (4)$$

According to Euler's rotation theorem [40], the coordinate system  $S_2$  is the result of rotating  $S_1$  about a fixed axis by a certain angle. Note that the coordinate system translation between  $S_1$  and  $S_2$  does not incur angular change. Hence, we denote the rotation axis and the angle from  $S_1$  to  $S_2$  as  $\mathbf{u}$  and  $\alpha$ , respectively.

To derive  $\mathbf{u}$  and  $\alpha$ , we select two reference vectors for  $S_1$  and  $S_2$ . Note that these reference vectors should not be parallel. These vectors should also not be parallel with  $\mathbf{u}$ . Our previous analysis provides us with six vectors in both  $S_1$  and  $S_2$ , i.e.,  $\mathbf{p}_1\mathbf{p}_2(S_1)$ ,  $\mathbf{p}_1\mathbf{p}_2(S_2)$ ,  $\hat{\mathbf{p}}_1(S_1)$ ,  $\hat{\mathbf{p}}_1(S_2)$ ,  $\hat{\mathbf{p}}_2(S_1)$ , and  $\hat{\mathbf{p}}_2(S_2)$ . According to Fig. 3(d),  $\mathbf{p}_1\mathbf{p}_2$  will not be parallel with  $\mathbf{u}$  when user moves. Therefore, we use  $\mathbf{p}_1\mathbf{p}_2$  as an reference vector, and denote  $\mathbf{p}_1\mathbf{p}_2(S_1)$  and  $\mathbf{p}_1\mathbf{p}_2(S_2)$  as  $\mathbf{D}_1$  and  $\mathbf{D}_2$ , respectively. Similar to the tracking algorithm of the 1-DoF joint, one should normalize  $\mathbf{p}_1\mathbf{p}_2(S_1)$  and  $\mathbf{p}_1\mathbf{p}_2(S_2)$ .

One can choose either  $\hat{\mathbf{p}}_1$  or  $\hat{\mathbf{p}}_2$  as another reference vector. In Fig. 3 (d), we use  $\hat{\mathbf{p}}_2$  as the reference vector. Ensuring that  $\hat{\mathbf{p}}_2$  and  $\mathbf{u}$  do not parallel during the measurement process can improve MagDot's tracking accuracy.

To achieve this goal, We change the orientation of MagDot #2's integrated magnet. As we will show in the hardware design of MagDot in Sec. 4, changing the orientation of the integrated magnet only needs to replace a 3D-printed holder. We denote  $\hat{\mathbf{p}}_2(S_1)$  and  $\hat{\mathbf{p}}_2(S_2)$  as  $\mathbf{Q}_1$  and  $\mathbf{Q}_2$ , respectively. Now, the rotation axis  $\mathbf{u}$  can be derived with the following equation.

$$\mathbf{u} = \frac{(\mathbf{D}_2 - \mathbf{D}_1) \times (\mathbf{Q}_2 - \mathbf{Q}_1)}{|(\mathbf{D}_2 - \mathbf{D}_1) \times (\mathbf{Q}_2 - \mathbf{Q}_1)|} \quad (5)$$

Here, we denote the coordinate of  $\mathbf{u}$  as  $(u_1, u_2, u_3)$ . Now, the rotation angle  $\alpha$  can be obtained by using:

$$\alpha = \begin{cases} \arccos\left(\frac{\mathbf{D}_{1\perp} \cdot \mathbf{D}_{2\perp}}{|\mathbf{D}_{1\perp}| \cdot |\mathbf{D}_{2\perp}|}\right), (\mathbf{D}_{1\perp} \times \mathbf{D}_{2\perp}) \cdot \mathbf{u} \geq 0 \\ -\arccos\left(\frac{\mathbf{D}_{1\perp} \cdot \mathbf{D}_{2\perp}}{|\mathbf{D}_{1\perp}| \cdot |\mathbf{D}_{2\perp}|}\right), (\mathbf{D}_{1\perp} \times \mathbf{D}_{2\perp}) \cdot \mathbf{u} < 0 \end{cases} \quad (6)$$

Here,  $\mathbf{D}_{1\perp}$  and  $\mathbf{D}_{2\perp}$  are the projections of  $\mathbf{D}_1$  and  $\mathbf{D}_2$  onto the plane perpendicular to the axis of rotation, respectively.

Applying the Rodrigues' rotation formula [40], the rotation matrix  $\mathbf{R}$  from  $S_1$  to  $S_2$  can be calculated by the rotation axis  $\mathbf{u}$  and rotation angle  $\alpha$ , as represented by the following equation.

$$\mathbf{R} = \mathbf{I} + (\sin \alpha)\mathbf{K} + (1 - \cos \alpha)\mathbf{K}^2 \quad (7)$$

where  $\mathbf{I}$  is the identity matrix and the matrix  $\mathbf{K}$  satisfies:

$$\mathbf{K} = \begin{bmatrix} 0 & -u_3 & u_2 \\ u_3 & 0 & -u_1 \\ -u_2 & u_1 & 0 \end{bmatrix} \quad (8)$$

Now, we can derive the value of  $\hat{\mathbf{v}}$  in  $S_1$  as follows.

$$\hat{\mathbf{v}}(S_1) = \mathbf{R}^{-1} \cdot \hat{\mathbf{v}}(S_2) \quad (9)$$

Finally, angles of the 2-DoF joint can be derived based on the following equations.

$$\begin{cases} \theta = \arccos(\hat{\mathbf{v}}(S_1) \cdot \mathbf{z}(S_1)) \\ \phi = \arccos((\hat{\mathbf{v}}(S_1) - (\hat{\mathbf{v}}(S_1) \cdot \mathbf{z}(S_1))\mathbf{z}(S_1)) \cdot \mathbf{x}(S_1)) \end{cases} \quad (10)$$

where  $\mathbf{x}(S_1)$  and  $\mathbf{z}(S_1)$  are the x-axis unit vector and the z-axis unit vector in  $S_1$ , respectively.



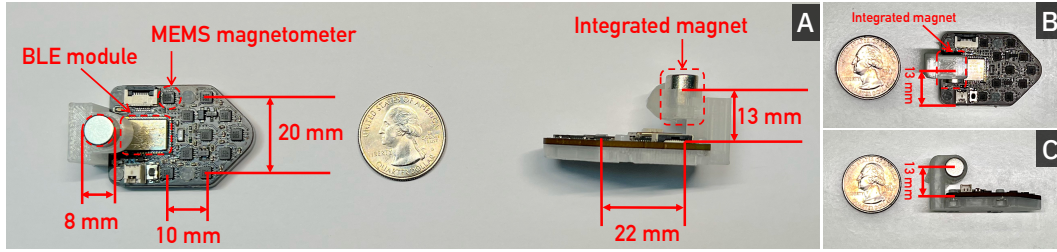


Fig. 4. The layout of MagDot’s magnet-integrated platform. (A) shows the sensing unit of 1-DoF tracking. (B) and (C) show the augmentation for 2-DoF tracking. Note that the change only needs to alter the 3D-printed holder.

### 3.3 Magnet-integrated Sensing Platform

MagDot’s high-accuracy joint tracking performance relies on two sensing units. Specifically, each MagDot unit combines a magnetic sensor array and a magnet, enabling simultaneous sensing and marking. The integrated design of MagDot allows it to track the passive magnet on another MagDot unit, while the embedded magnet marks its position for the other unit to track. The layout of the MagDot platform is shown in Fig.4, where the magnet and magnetic sensor array are fixed together with a 3D-printed holder to ensure stability. We will elaborate on the hardware configuration in Sec.4. Next, we will introduce the calibration and magnetic tracking techniques of the MagDot platform.

**3.3.1 Calibration method.** It is crucial to address the inherent magnetic noise [60] in the sensor array. To mitigate these errors, we adopt the spherical fitting algorithm [47] to obtain the hard-iron and soft-iron coefficients, which are utilized to calibrate the sensor readings.

To eliminate the constant magnetic bias induced by the integrated magnet near the sensor array, we employ the hard-iron calibration method described in [60]. This involves acquiring bias correction data while MagDot is kept stationary and away from other magnets. We then subtract the mean value of the bias correction data from the sensor readings. This process eliminates the impact of the integrated magnet on all the sensors and ensures accurate tracking performance.

Although the bias correction data also includes background magnetic field component, the tracking results remain unaffected. Specifically, after the calibration process, we can denote the magnetic field  $\mathbf{B}$  detected by the sensor in the following formula.

$$\mathbf{B} = \mathbf{B}_m + (\mathbf{G} - \mathbf{G}_0) \quad (11)$$

where  $\mathbf{B}_m$  is the magnetic field generated by the targeted magnet;  $\mathbf{G}$  is the real-time environment magnetic field, e.g., earth’s magnetic field;  $\mathbf{G}_0$  is the environment magnetic field recorded in the calibration phase.  $(\mathbf{G} - \mathbf{G}_0)$  casts a uniform magnetic field on all sensors, which is different from the non-uniform magnetic field generated by the passive magnet. Therefore,  $\mathbf{G}_0$  does not affect the tracking results.

**3.3.2 Magnetic tracking principle.** After the calibration step, MagDot needs to eliminate the effects of the background magnetic field while focusing on the magnetic field generated by the target magnet. Here, the background magnetic field refers to a uniform magnetic field (e.g., Earth’s magnetic field) with the same magnetic field strength that projects on each sensor in the sensor array. The target magnet, on the other hand, is the passive magnet attached to the other MagDot unit. To characterize the magnetic field of the target magnet, we use the dipole model [55] as indicated by the following equation.

$$\mathbf{B}_m = \frac{\mu_0}{4\pi} \left( \frac{3(\mathbf{m} \cdot \mathbf{r})\mathbf{r}}{|\mathbf{r}|^5} - \frac{\mathbf{m}}{|\mathbf{r}|^3} \right) \quad (12)$$

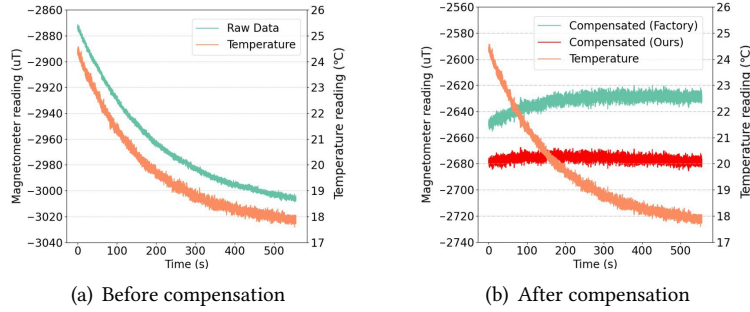


Fig. 5. Magnetometer reading and temperature variation before and after MagDot’s thermal drift compensation. In (b), the “Factory” curve represents the compensated data using MLX90393 suggested coefficient, while “Ours” curve refers to the compensated data utilizing the coefficient calculated by MagDot.

where  $\mathbf{m}$  is the magnetic moment and encompasses the orientation parameters of the magnet;  $\mathbf{r}$  is the displacement vector from the magnet to the observation point and comprises the position parameters of the magnet.

Based on the readings of MagDot’s magnetometer array, we can construct a nonlinear optimization function that includes parameters, i.e., the position and orientation of the target magnet and the strength of the background magnetic field. Specifically, for sensor  $i$  ( $i = 0, 1, \dots, n$ ;  $n$  is the sensor number of array), the loss function  $E_i$  is defined by the following equation.

$$E_i = \left[ \frac{\mu_0}{4\pi} \left( \frac{3(\mathbf{m} \cdot (\mathbf{r}_i - \mathbf{r}_m)) (\mathbf{r}_i - \mathbf{r}_m)}{|\mathbf{r}_i - \mathbf{r}_m|^5} - \frac{\mathbf{m}}{|\mathbf{r}_i - \mathbf{r}_m|^3} \right) + (G - G_0) \right] - B_i \quad (13)$$

Here,  $B_i$  is the sensor reading, and  $\mathbf{r}_m$  represents the magnet’s position;  $\mathbf{r}_i$  denotes the position of sensor  $i$ , which is known in advance.

Next, we employ the Levenberg-Marquardt algorithm [41] to determine the position and orientation of the target magnet. For detailed steps of magnetic tracking, readers can refer to [21].

### 3.4 Thermal Drift Compensation

MEMS magnetometers contain magnetoresistive elements in a small package and are sensitive to temperature changes [43, 45]. Thermal fluctuations can cause sensor sensitivity to change, which cannot be neglected for common commercial off-the-shelf (COTS) magnetometers. For example, the LIS2MDL magnetometer [1] has sensitivity fluctuations up to 7%, whereas the MLX90393 [6] can encounter variations of up to 3%. This effect can be particularly challenging when the magnetometer readings are large.

We conducted an empirical study to analyze the thermal drift in MEMS magnetometers, i.e., the MLX90393 sensor in this paper. We placed our magnet-integrated platform inside an HN-25BS temperature chamber. The nearby magnet generated a high sensor reading of approximately  $3700 \mu T$ . The chamber had no magnetic interference, meaning the environment’s magnetic field was constant when we tuned the temperature. This allowed us to observe the magnetometer’s temperature drift. We inspected the y-axis data of the magnetometer. We found that the readings showed significant drift, decreasing from  $-2870 \mu T$  to  $-3010 \mu T$  under a small temperature change of approximately  $6^\circ C$ , as shown in Fig. 5(a). To verify the variance is not incurred by the magnet’s temperature change, we heated the integrated magnet to  $60^\circ C$  and placed it back. The change was only around  $20 \mu T$ , indicating that this variation is caused by the magnetometer’s internal drift.

To verify temperature drift's impact on tracking accuracy, we used a magnetometer to sense the magnet's magnetic field at different distances. The results showed that when the magnet-sensor distance was approximately 8 cm, the magnet's field strength degraded to  $43 \mu T$ , which is much smaller than the temperature drift as shown in Fig. 5(a). As a result, the temperature drift can lead the LM tracking algorithm to converge to an incorrect position, severely impairing tracking accuracy.

To compensate magnetometer's temperature drift, existing methods uniformly shift the raw magnetometer readings to the values at a reference temperature. The core idea is based on the following formula:

$$\mathbf{B}_{corr} = \mathbf{B}_{raw} (1 + \mathbf{k} (T - T_{ref})) \quad (14)$$

where  $\mathbf{B}_{raw}$  and  $\mathbf{B}_{corr}$  are the sensor readings before and after compensation, respectively.  $T$  is the temperature measured by the magnetometer.  $\mathbf{k}$  denotes the compensation coefficient for each axis of the magnetometer.  $T_{ref}$  represent a reference temperature. For MLX90393, manufacturer set  $T_{ref}$  at  $35^\circ C$ .

However, the degree of thermal sensitivity can vary depending on the specific sensor and even between the different axes of the same sensor. Therefore, a universal constant, i.e.,  $\mathbf{k}$ , is ill-fitted for addressing the temperature drift in high-precision sensing tasks.

To mitigate the impact of the thermal drift and ensure robust tracking performance, we introduce a novel approach to derive the coefficient vector for each sensor. Specifically, we collect a small amount of data for only a few minutes and use a least squares algorithm to adjust the coefficient vector. To demonstrate the efficacy of our design, we conducted an empirical study. We first collected data from a magnetometer with a temperature change over time while maintaining a constant magnetic environment. Therefore,  $\mathbf{B}_{corr}$  remained unchanged during measurement. Next, we utilized the collected  $T$  and  $\mathbf{B}_{raw}$  of each axis to derive, using the least squares method, the unknown constants  $\mathbf{B}_{corr}$  and  $\mathbf{k}$  for every axis.

$$\min_{\mathbf{k}, \mathbf{B}_{corr}} \sum_{i=1}^N [\mathbf{B}_{raw,i} (1 + \mathbf{k} (T_i - T_{ref})) - \mathbf{B}_{corr}]^2 \quad (15)$$

After solving the compensation coefficients for each axis of every magnetometer, we can compensate for the drift of raw readings. We first process the same data of Fig. 5(a) with the suggested coefficient given by [9], which is 0.007328. As shown in Fig. 5(b), we can still observe a substantial drift of around  $25 \mu T$  which poses trouble in magnetic tracking. By using our compensation scheme, we can clearly observe that the compensated data remains stable without drifting. Note that this procedure is a one-time effort, e.g., a factory setting, which is essential for assuring the usability of MagDot.

### 3.5 Skin Deformation

Skin deformation and soft tissue artifacts can lead to tracking errors. The deviation of the sensor orientation from the bone axis is a common problem that can affect tracking accuracy [31]. As a result, these effects can alter the position and orientation of the MagDot units.

**3.5.1 Error analysis.** According to Sec. 3.1 and Sec. 3.2, the translation between the coordinate systems of the two MagDot units does not undermine the tracking performance. Therefore, the position error only incurs minimal impact to MagDot.

Now we analyze the orientation error. As illustrated in Fig.3 (a), MagDot units can have orientation changes in three directions, i.e., rotations around the x, y, and z axes, respectively. Therefore, if left unattended, the orientation error incurred by skin deformation can undermine the accuracy of tracking results in different orientations. Based on our empirical studies, orientation changes caused by skin deformation can be mitigated by placing the MagDot units on bony landmarks [13, 57]. This placement strategy can help capture the anatomical frame of the joint. Note that this guideline also aligns with existing methods in Mocap techniques, i.e., wearing reflective markers.

To further reduce the impact of orientational error, we propose a skin deformation compensation method with minimal overhead.

**3.5.2 Compensation method.** First, we attach the MagDot units on the joint and move it to the zero-degree position (e.g., full extension) to record the tracking result as a constant bias. This step helps remove the initial orientation deviation of MagDot units. Next, we move the joint to a specific landmark angle and record the tracking result. Based on our empirical observations, a larger landmark angle usually leads to better compensation performance. We derive the compensation factor for skin deformation by dividing the value of the landmark angle by the tracking result. Finally, we subtract the bias from the tracking result and multiply it by the compensation factor to eliminate the influence of skin deformation. In MagDot, we tackle skin deformation as a linear offset to the joint angle. Based on our empirical studies, we found the linear model is a practical approximation for characterizing the impact of skin deformation. Specifically, the joint's skin curvature varies continuously as the angle changes. The extent of deformation also correlates with the joint angle. For example, when the joint angle is slight, e.g., elbow extension, the skin deformation is mild. When the user's joint bends, e.g., elbow flexion, the flexing muscle leads to a large skin deformation. We will demonstrate its efficacy via experiments in Sec. 6.

Our skin deformation compensation method is a one-time process for each joint. However, it may need to be reconfigured if users track other joints or experience significant changes in body shape, such as weight gain or loss. We believe that the overhead incurred by the compensation process is minimal for users, given that the change in body shape is a long-term process.

## 4 HARDWARE DESIGN OF MAGDOT

To assure the accuracy and wearability of MagDot, the hardware architecture of the MagDot consists of several constituent elements, including a sensor array, data processing circuits, an integrated magnet, and a 3D-printed holder. The following is a detailed introduction to our hardware design.

### 4.1 Layout Design

In the layout design, we need to determine two key hardware metrics: (1) the relative position between sensors; (2) the distance between the sensor array and its corresponding integrated magnet. To assure MagDot's performance, we propose the following design principles:

- (1) **Maximizing tracking range.** To maximize the tracking range of system, the distance among sensors should be sufficient to capture the magnetic field at a broader range. This can improve the diversity of sensor reading between different sensors, thus allowing the LM algorithm to derive an accurate location of the targeted magnet. Therefore, a sufficient area of the sensor array layout is recommended.
- (2) **Minimizing readings noise.** Although the integrated magnet can enable a usable form factor, it may saturate its corresponding sensor array. For example, according to our empirical study for the MLX90393, with a reading of  $50 \mu T$ , the standard deviation of the sensor reading is  $0.4 \mu T$ . When the sensing reading reaches  $6000 \mu T$ , the standard deviation increases to  $12 \mu T$ . In the MagDot sensing unit design, one should keep a distance between the integrated magnet and sensor array.
- (3) **Compact form factor.** A compact form factor is critical for facilitating the wearability of MagDot. Small size can also mitigate the incidence of collisions between two MagDot units.

Principles #1 and #2 lead to a loose form factor, whereas principle #3 requires a compact design. In the design of MagDot, we determine the arrow-shaped sensor configuration of MagDot. The sensor array includes ten magnetic sensors and arranges in two parallel arrow-shaped layouts, with each sensor cluster containing five magnetometers. The arrow-shaped design help minimize the possibility of collision between two sensing units. As shown in Fig. 4, The width and length of each arrow are  $2 \text{ cm}$  and  $1 \text{ cm}$ , respectively. The distance between

two arrows is 1 *cm*. We place the integrated magnet at the rear end of the platform. Specifically, the horizontal distance and height of the magnet from the front of the unit are 3.2 *cm* and 1.3 *cm*, respectively. The efficacy of our design is validated with our benchmark study in Sec. 5 and on-body tests in Sec. 6, demonstrating that the proposed layout effectively achieves high tracking accuracy while maintaining ease of use.

## 4.2 Hardware Configuration

**4.2.1 Sensor setup and circuit design.** We choose MLX90393 magnetometers since this model has a large measurement range (i.e., 5 - 50 *mT*) to avoid saturation. It also has an onboard temperature sensor to support the temperature compensation algorithm. To avoid saturation, we apply the following configurations of the magnetometer. We set resolutions of *x*, *y*, and *z* axis as 0.150 *uT*, 0.150 *uT*, and 0.242 *uT*, respectively. The measurement ranges of *x*, *y*, and *z* axis are 4920 *uT*, 4920 *uT*, and 7930 *uT*, respectively. Finally, we tune the noise thresholds of *x*, *y*, and *z* axis under 1.1 *uT*, 1.1 *uT*, and 0.6 *uT*, respectively.

For circuit design, we use a Bluetooth Low Energy module MDBT42Q [2] as the microcontroller, which communicates with our 10-magnetometer array via SPI protocol. We set the sample rate of the magnetometer to 16 *Hz*. The collected sensor readings will be sent to the computing unit for further processing via BLE. Specifically, We used a Thinkpad X1 laptop (with Intel Core i7-10510U CPU) as the computing unit. We mount the components on a customized four-layer printed circuit board (PCB). The circuit schematic is shown in Fig. 6. To further reduce the size of the PCB, we integrate the flashing-related components (i.e., CP2104 chip, USB port) onto another board. To enable flashing, we use a dedicated flexible printed circuit (FPC) connector. In comparison to existing joint tracking methods, the hardware of MagDot, including sensors, BLE module, and manufacturing cost, incurs minimal expenses — each MagDot unit costs less than \$35.

**4.2.2 Magnet configuration and 3D-printed holder design.** For the integrated magnet, we use the neodymium-iron-boron (NdFeB) passive magnet [10]. This material can incur sufficient magnetic field with low cost and compact size. The shape of the integrated magnet is determined to be cylindrical for ease of fixation. Both the diameter and height of the integrated magnet are 8 *mm*. To maintain the relative static configuration between the sensor array and the integrated magnet, we fabricate a 3D-printed holder. The integrated magnet is embedded in the holder. The PCB of the sensing platform is fixed to the holder with plastic screws, as shown in Fig. 4.

## 5 BENCHMARKS

Now we benchmark MagDot's performance, i.e., tracking accuracy, temperature compensation, and energy cost. Then, we compare MagDot's performance with that of an IMU-based method under different interferences.

### 5.1 Tracking Accuracy of MagDot

We designed 1-DoF and 2-DoF joint models to facilitate an accurate and cost-efficient testing process. Specifically, our design leveraged the characteristic features of hinge and ball-and-socket joints on the human body. Next, we fabricated these joint models with 3D printer. As shown in Fig. 7, MagDot units can be placed on the models' bases and align well with the joint axis. The distances between the two MagDot units on the 1-DoF and 2-DoF models are 7.5 *cm* and 7.0 *cm*, respectively.

**5.1.1 Ground Truth Collection.** To acquire the precise angles of joint models, we employ an optical motion capture device, i.e., the Leap Controller. It can capture the position and orientation of the tip of a pen-like object, with an average accuracy of 1.2 *mm* [63]. The overall setup for the platform is depicted in Fig. 7.

**5.1.2 1-DoF Joint.** We placed two MagDot units on the 1-DoF joint model. Next, we moved the joint model from 0° to 120°, and then returned to 0°. We repeated the process five times. Fig. 8 (a) presents the result during a single movement process. Fig. 8 (b) shows the error distribution on different angle ranges. Fig. 8 (b) uses the



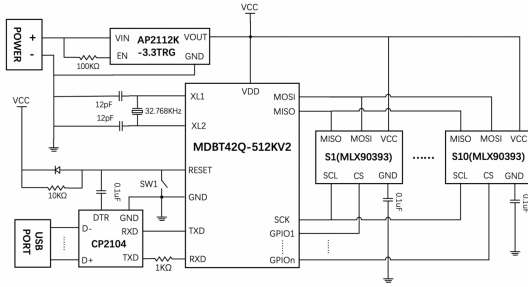
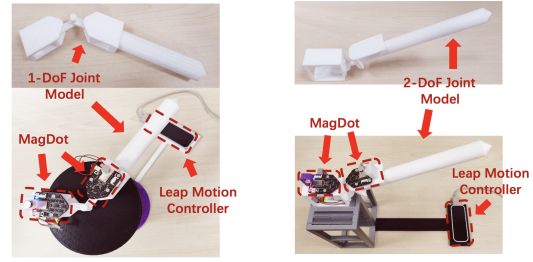


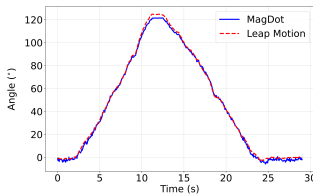
Fig. 6. The circuit schematic of MagDot.



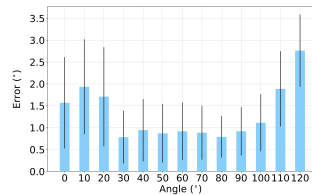
(a) 1-DoF joint

(b) 2-DoF joint

Fig. 7. Experimental setup with Leap Motion controller.



(a) Tracking trace



(b) Tracking error

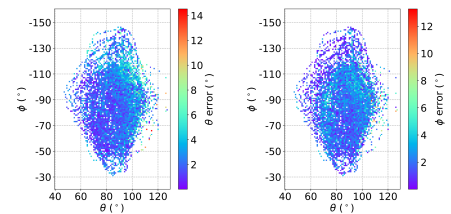
(a) Error of  $\theta$ (b) Error of  $\phi$ 

Fig. 8. The error distribution of the 1-DoF joint.

Fig. 9. The error distribution of the 2-DoF joint.

data of all five repetitions. Each bar has over one hundred points. Here, the bar at  $0^\circ$  denotes the mean error and standard deviation of MagDot when the angle varies between  $-5^\circ$  and  $5^\circ$ .

Based on Fig. 8 (a), the root mean square error (RMSE) of MagDot are  $1.82^\circ$ . As shown in Fig. 8 (b), when the angle of the 1-DoF joint model is around  $30^\circ$ , the average tracking error is only  $0.78^\circ$ , with a standard deviation of  $0.6^\circ$ . Due to the increased distance, the maximum error appears when the joint model moves between  $115^\circ$  to  $125^\circ$ . MagDot can still achieve an average error of  $2.76^\circ$  and a standard deviation of  $0.83^\circ$ .

**5.1.3 2-DoF Joint.** In this experiment, we rotated the distal segment of the 2-DoF joint model around the joint center arbitrarily to assess the accuracy of the tracking algorithm. In total, we collected 10,960 data points. The experimental result is shown in Fig. 9. Specifically, 2-DoF joint tracking exhibits high accuracy. The angle ranges on  $\theta$  and  $\phi$  are  $47^\circ$  to  $126^\circ$  and  $-146^\circ$  to  $-29^\circ$ , respectively. The RMSEs of  $\theta$  and  $\phi$  are only  $2.98^\circ$  and  $2.80^\circ$ , respectively. Furthermore, as  $\theta$  increases gradually, both  $\theta$  and  $\phi$ 's tracking performance degrade. This is because, as  $\theta$  increases, the distance between MagDot and the target magnet increases, thus undermining the tracking performance.

## 5.2 Drift Analysis of MagDot

Now, we analyze the drift performance of MagDot. To quantify the drift effect in the long-term use of MagDot, we fixed MagDot on a wooden board at an angle of  $0^\circ$ . Note that  $0^\circ$  denotes joint extension — a representative angle in joint tracking applications. We performed a continuous angle-tracking task in the experiment for up to four hours. To emulate the real-world usage that may lead to large drift errors, we performed three different motions. (1) rotating the board around the x,y, and z axis; (2) carrying the board while walking in a living room; (3) carrying the board while climbing stairs. As highlighted in Fig. 10, each motion was performed at the end of

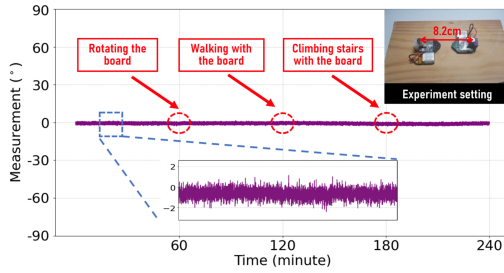


Fig. 10. The tracking result under four hours of continuous experiment. An action is performed once per hour.

one, two, and three hours. The time duration of each motion was 2 minutes. Fig. 10 presents the tracking result throughout the experiment. MagDot can keep a constant tracking accuracy, with the mean error and standard deviation as  $0.79^\circ$  and  $0.42^\circ$  even in the last five minutes, thus demonstrating its drift-free and robust tracking performance in real-world, long-term usage.

### 5.3 Temperature Compensation Method

We divide the experiment into two groups. In the first “compensation group”, the magnetometer raw readings are first compensated for thermal drift using Eq. 14 before being used for subsequent algorithm processing, i.e., calibration and tracking algorithm. For the “uncompensated group”, the raw readings are directly used for algorithm processing. We first conducted a tracking accuracy test for both groups immediately after calibration. Then we simulated changes in room temperature by activating the air conditioning, resulting room temperature to increase about  $2^\circ\text{C}$ . After that, we repeated the accuracy test for both groups.

Fig. 11 shows the tracking error. Before manually introducing thermal change, for both compensated and uncompensated cases, the tracking results are stable. However, when the temperature changes, i.e., only  $2^\circ\text{C}$ , the thermal drift in the magnetometer introduces substantial error in the LM algorithm. This result demonstrates the MagDot’s thermal compensation can effectively stabilize the tracking accuracy. Here, the tracking result with the compensated sensor reading only has  $1.06^\circ$  higher overall error at  $120^\circ$ .

### 5.4 Energy Cost

We profile the energy consumption of MagDot by measuring the battery supply voltage and current. It shows an average of  $98\text{ mW}$  power drain on a single MagDot unit. Thus, our small-size, low-capacity lithium battery ( $3.7\text{ V}$ ,  $220\text{ mAh}$ ) can ensure continuous operation for up to  $8\text{ hours}$ .

### 5.5 Comparison with IMU

We conducted a comparative evaluation of MagDot with a high-end IMU sensor, the XSens IMU [5], which is known for its superior performance compared to low-cost IMUs, such as those found in smartphones. Our evaluation procedure involved subjecting both sensors to acceleration and magnetic interference, as described in Sec. 2.2. The experimental settings are shown in Fig. 12. Note that XSens IMU is a proprietary commercial product whose hardware is not reconfigurable. To employ XSens IMU for joint tracking, we strictly comply to the usage instructions and guidelines provided by XSens IMU user manual [5].

**5.5.1 Acceleration.** Large linear acceleration will distort the accelerometer reading, therefore miscalculating the current attitude. In contrast, our platform is immune to the acceleration influence.

As depicted in Fig. 12 (a), we predetermine an angle and examine whether MagDot and XSens can accurately track the angle. First, we fixed both ends of a goniometer on a wooden board, keeping the joint angle at  $0^\circ$ . Next,

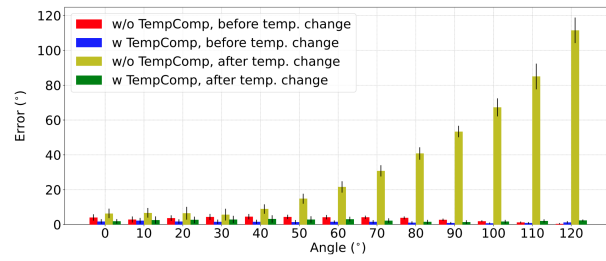


Fig. 11. The joint tracking results with and without temperature compensation, before and after the temperature change.

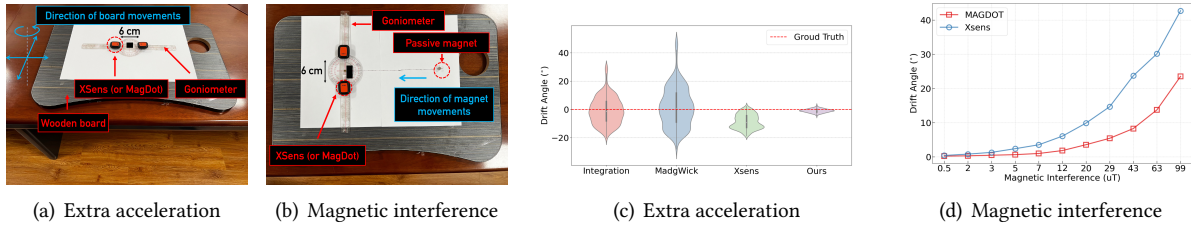


Fig. 12. Comparison of angle tracking accuracy in the presence of extra acceleration or magnetic interference. (a) and (b) present the experiment settings of acceleration and magnetic interference, respectively.

we attached two XSens on both of the goniometer. This formulates a  $0^\circ$  angle between two XSens units. To introduce additional acceleration, we conducted controlled movements by sliding the board on a flat surface for 30 seconds. It is important to note that the motion excluded the effect of gravity, meaning that only free acceleration on the XY-plane was induced in the experiment. Since the IMUs were positioned on the horizontal plane, only the angle rotating along the Z-axis (i.e., the yaw angle) would change. To obtain the measured angle, we subtracted the yaw angle measured by one IMU from the other. For MagDot, we replicated the same setup by attaching two platforms to both ends of the goniometer.

We choose three ways to calculate the angle based on the IMU data. **1) Integration.** We obtain the angle by integrating the raw gyroscope data of XSens. **2) Madgwick algorithm.** We obtain the raw data of XSens and leverage the classic fusion algorithm Madgwick [38] to calculate the 3D orientation. We follow the same parameter settings as [38]. **3) XSens' proprietary method.** We use the Euler angle output of Xsens generated by the built-in sensor fusion algorithm XKFCore [5].

We demonstrate the tracking performance with a violin plot in Fig. 12 (c). For the integration method, despite being a high-end COTS IMU, XSens' raw data shows a large drift in the angular measurement. The Madgwick algorithm performs worst as it calibrates the gyroscope drift using the polluted acceleration data. The built-in algorithm of XSens has the best performance of all IMU-based approaches. Yet, it still shows a large angular error of up to  $20^\circ$ . In contrast, MagDot shows the best resilience against acceleration. Specifically, the deviation is only  $1.47^\circ$  after 30 seconds, with a mean deviation of  $2^\circ$  during the whole movement. Our on-body results (Sec. 6) also demonstrate MagDot's efficacy.

**5.5.2 Magnetic Interference.** The magnetic interference can overpower the common ambient magnetic field (e.g., the earth's magnetic field), thus polluting the direction estimation for IMUs. Our algorithm for tracking the magnet can differentiate the targeted magnet's field from the residual ones, thus improving the robustness of the tracking performance.

XSens provides a magnetic field mapping (MFM) procedure [4] to compensate for the magnetic disturbances. However, this procedure is cumbersome as the user has to move the IMU device with constant speed along x, y, and z directions for a few minutes. The user needs to iterate the MFM procedure when the magnetic field changes, thus severely limiting the usability of IMU-based tracking.

In the experiment, we followed a similar procedure of placing the goniometer, IMUs, and MagDot units as shown in Sec. 5.5.1. As depicted in Fig. 12 (b), to emulate the impact of magnetic disturbance, we moved a permanent magnet gradually toward the goniometer. The distance between the magnet and the center of the goniometer changes from  $25\text{ cm}$  to  $6\text{ cm}$ . To quantify the magnetic field disturbance, we measured the magnetic field strength at the center of the goniometer. The strength of magnetic disturbance ranges from  $0.5\ \mu\text{T}$  to  $99\ \mu\text{T}$ . This is common in daily life, e.g., an iPhone 12 Pro can incur around  $40\ \mu\text{T}$  in a distance of  $3\text{ cm}$  [51]. We use the










Magnetic interferences	No disturbance	Wireless earphone	Wireless mouse	Smart wristband	Bone conduction earphone	Smartphone	Laptop	Metal chair	Metal writing desk
Settings									
Err.(Mean,std)	(0.76,0.26)	(0.85,0.30)	(0.64,0.24)	(0.76,0.25)	(6.90,5.16)	(1.16,0.38)	(2.42,0.52)	(2.00,1.39)	(4.78,3.77)

Fig. 13. The tracking error of MagDot under real-world magnetic interference. The unit of angular error is degree.

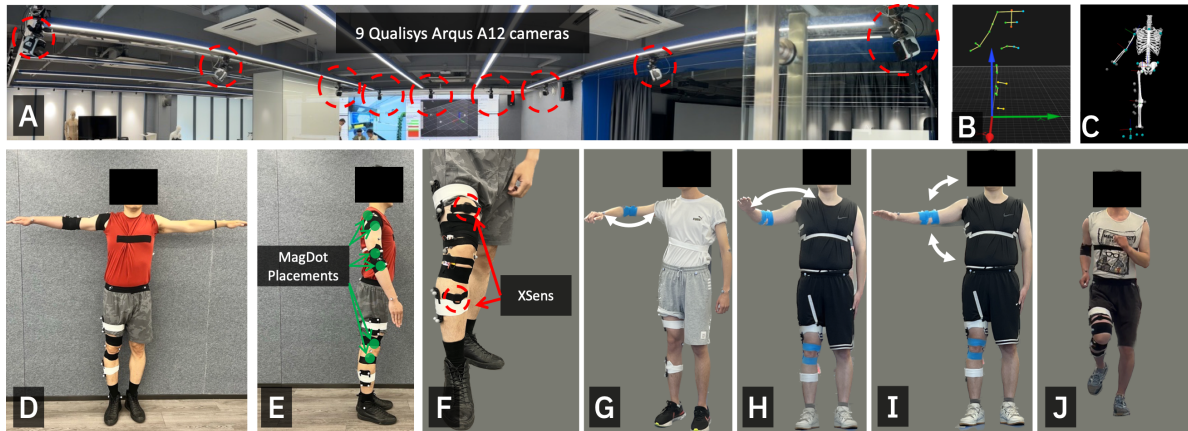


Fig. 14. Experiment settings of the on-body test with Qualisys motion capture system. (A) is the panoramic of the Qualisys mocap system; (B) shows the tracked markers in the QTM software; (C) presents the reconstructed kinematic model in Visual3D; (D), (E), and (F) shows the placements of reflective markers, MagDot units and XSens trackers, respectively; (G) – (J) shows elbow movement, elbow transversal movement, elbow's frontal movement, and running trial, respectively.

Madgwick algorithm to derive the angle with IMUs. As shown in Fig. 12 (d), MagDot outperforms the IMU. For example, under  $40 \mu T$  disturbances, MagDot's error is only half of the IMU approach.

Now we evaluate MagDot's resilience against magnetic interference in the real world. To emulate the interference, we use common ferromagnetic objects, e.g., smartphones, earbuds, laptops, and metal furniture. In our experiment, we fixed two MagDot units at an angle of  $0^\circ$ . Then, we moved magnetic objects close to our sensing units. The closest distance was  $6cm$ . We quantified the interference by measuring the tracking error. As shown in Fig. 13, MagDot only shows minimal performance degradation with real-world interference.

Our benchmark studies help iterate the design of MagDot. Due to the high cost of on-body experiments and mocap systems, we believe our benchmark procedure is valuable for fast-prototyping joint-tracking applications.

## 6 ON-BODY EVALUATIONS

Now, we perform rigorous on-body experiments to evaluate performance in real-world applications. First, we assess the tracking capabilities of MagDot on representative 1-DoF and 2-DoF joints, such as the elbow and shoulder joints, respectively. Next, we compare MagDot with state-of-the-art IMU-based approaches in a real-world joint tracking application, i.e., gait analysis. Our studies received approval from the university's IRB review board for all procedures involved in our experiment.

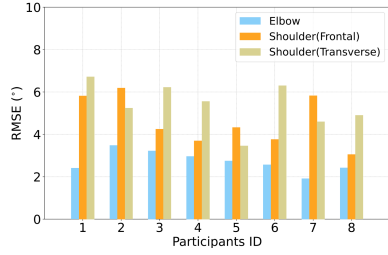


Fig. 15. 1-DoF and 2-DoF tracking results of MagDot.

Table 1. Information of all participants

ID	Height (m)	Mass (kg)	BMI
1	1.77	60	19.24
2	1.68	65	23.03
3	1.78	66	20.83
4	1.91	85	23.30
5	1.82	80	24.15
6	1.75	68	22.20
7	1.72	64	21.63
8	1.86	88	25.43

## 6.1 Experiment Setting

**6.1.1 Data Collection.** To accurately evaluate MagDot’s tracking capabilities, we used a high-precision, full-fledged mocap system to record the ground truth. Fig. 14(A) shows the mocap system consisting of nine QualiSys infrared cameras (Arqus A12 [12]) with a 3D tracking resolution of 0.04 mm. Reflective markers were attached to the joints by a professional mocap engineer (Fig. 14(D)), following the CAST body marker set placement guidelines of Qualisys [13, 56]. During the experiment, the mocap system recorded the spatial coordinates of the markers and fed them into Visual 3D software [15], i.e., a professional 3D motion analytics tool for biomechanical research. Next, we reconstructed skeleton models and kinematic models of participants as shown in Fig. 14(B), and Fig. 14(C). These models could yield the angular changes of each joint. In this experiment, we selected the elbow, shoulder, and knee on the right side. The mocap system’s sampling frequency is 100 Hz. We used timestamps and linear interpolation to match ground truth with MagDot’s results.

**6.1.2 Participants.** To demonstrate the accuracy and usability of MagDot, we recruited eight participants with varying body mass indices — ranging from 19.2 (healthy) to 25.5 (overweight) — and ages between 21 and 32. Prior to the experiment, we provided instructions to the participants on how to move their joints to collect data for skin deformation compensation, as explained in Sec. 3.5. Attaching MagDot to the user’s joints can be achieved using various approaches such as kinesiology tape, cohesive tape, glue dot, or transparent medical tape. In the experiment, we used KT tape [7], a widely used elastic tape in rehabilitation, to attach MagDot units to the participants’ joints. One can also use the medical tape as shown in Fig. 1. Our results in Fig. 20 demonstrate that different attachment methods do not compromise the tracking performance of MagDot.

## 6.2 1-DoF Tracking

We first evaluated the performance of MagDot on the elbow joint and verified the accuracy of its 1-DoF tracking algorithm. All eight participants were asked to flex and extend their elbows repeatedly to the straight position for 50 seconds. To assess the robustness of MagDot’s skin deformation compensation method, we conducted one remount experiment where a participant was instructed to remove MagDot units and then reposition them *without* recalibrating the skin deformation. That is, the compensation coefficient of the initial placement was used for the repositioned units. The participant then continued to flex and extend the elbow for another 50 seconds.

The results of our experiments demonstrate the accurate and stable tracking performance of MagDot. As depicted in Figure 15, MagDot achieves high tracking accuracy on all participants with an average root mean square error (RMSE) of 2.72°. To further illustrate the stability of MagDot, we show the tracking curvature of participant #7 in Figure 16 (a) as an example. In this experiment, the participant flexes and extends the elbow repeatedly for 50 seconds, and MagDot accurately tracks the movement without drift, as indicated by the consistent tracking curvature. We also conducted a remount experiment to test the robustness of our skin deformation



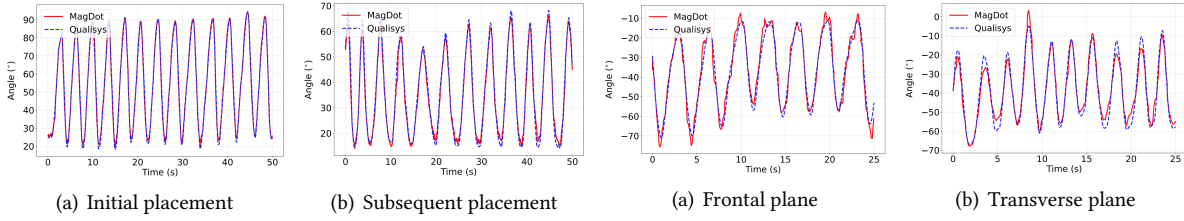


Fig. 16. Tracking result of elbow joint with MagDot.

Fig. 17. Tracking results of shoulder joint with MagDot.

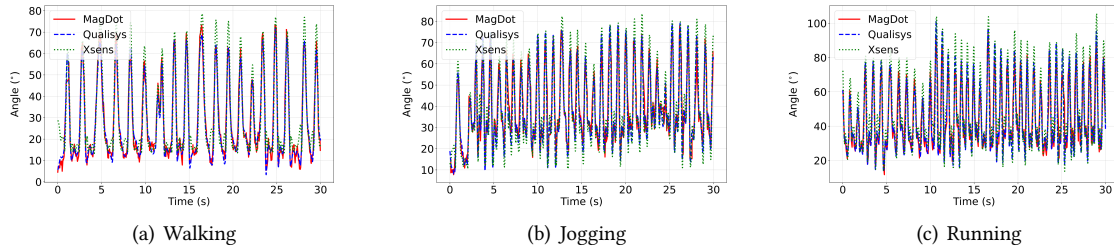


Fig. 18. Tracking results of the knee joint under different motion states. We compared MagDot with QualiSys and XSens.

compensation method. After repositioning MagDot, it achieves an RMSE of  $2.05^\circ$ , which is comparable to the initial placement. The consistent performance in Figure 16 (b) further demonstrates the robustness of MagDot.

### 6.3 2-DoF Tracking

To evaluate MagDot's performance in tracking 2-DoF joints, we conducted experiments on the shoulder joint. All eight participants were instructed to perform two motions: (1) raising their arms in the frontal plane, and (2) extending their arms in the transverse plane. Each motion was repeated for 25 seconds.

Fig.15 illustrates the tracking performance of both shoulder movements. From all participants, MagDot achieves an overall RMSE of  $4.61^\circ$  for the frontal plane and  $5.38^\circ$  for the transverse plane. As an example of the continuous trajectory of the angular data, we plot participant #5's data in Fig.17. This result demonstrates MagDot maintains high accuracy without drifting. It is worth noting that the 2-DoF joint tracking performance is relatively inferior to that of 1-DoF cases due to larger skin deformation. However, this level of accuracy is still sufficient for many scenarios. For instance, in clinical practice, the maximum measurement error for joint flexion using a goniometer has been reported to be  $7^\circ$  [20].

### 6.4 Gait Analysis

Measuring knee movements with precision is the key to analyzing gait patterns and inefficiencies, particularly in sports and medical studies [17, 65]. However, existing precise gait analytics requires high-cost equipment, e.g., XSens IMUs. Unfortunately, these costly approaches still suffer from high drifting error. In contrast, MagDot can *enable high-precision gait measurement at an extremely low cost*. To evaluate MagDot's accuracy in gait analysis, we attached two units on the knee joint and instructed all eight participants to sequentially run, jog, and walk for 30 seconds each. We also attached two XSens DOT IMUs to the participant's shank and thigh to compare MagDot's performance with IMU-based gait analysis. We keep a sufficient distance between IMU and our platforms to assure MagDot's magnet would not affect XSens units. We derived the knee angle from the IMUs' 3D orientation

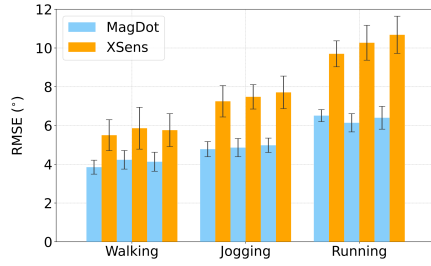


Fig. 19. The performance of MagDot and XSens over time.

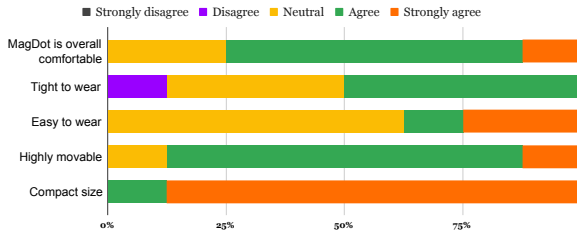


Fig. 21. The user study of MagDot's comfortableness by calculating the relative angle of the two x-axes in the global frame, which aligned with the shank and thigh. We calibrated XSens' IMU units before the gait experiment. Specifically, each participant was instructed to perform calibration posture by standing for 10 seconds. The data from this time interval can align IMU's local coordinate with the corresponding body segment's coordinate.

Based on the empirical results, MagDot provides accurate tracking performance of the knee joint motion on all eight participants, with overall RMSE of  $4.14^\circ$ ,  $4.88^\circ$ , and  $6.32^\circ$  for walking, jogging, and running, respectively. In contrast, the IMU exhibits fluctuating tracking performance with average RMSEs of  $5.71^\circ$ ,  $7.53^\circ$ , and  $10.27^\circ$  for the same movements. As an example, we plot participant #8's MagDot and XSens data in Fig. 18. MagDot shows high tracking accuracy despite the variance of moving patterns.

Fig.19 compares the impact of drifting errors on gait analysis using MagDot and IMU-based methods. We used all participants' data. Next, we divide each participant's data into three 10-second time slots for analysis of each movement pattern. Then, we aggregate the mean and STD values of each movement's RMSE, and present Fig.19. Our experiment presents three key findings: (1) MagDot exhibits consistent performance that is invariant to time, indicating that it is drift-free. (2) IMU-based methods show aggregating drift error in all movement patterns. (3) IMU-based techniques show severe drift in more intense movements. This pattern indicates that the state-of-the-art IMU approach is susceptible to varying acceleration, consistent with Sec.2.2. More intense moving patterns may also undermine MagDot's performance. The reason is that intense movement can lead to larger skin deformation and vibration.

## 6.5 Wearability of MagDot

There are several methods for attaching MagDot to joints. Here, we compare tracking accuracy between KT tape and medical tape. We used a transparent medical tape that was 1 cm in width, as shown in Fig.1, to attach MagDot to the joints. We invited the first two participants and evaluated the tracking performance of their elbow joints. The data collection process was the same as outlined in Sec.6.1. Our results, presented in Fig.20, demonstrate that the lightweight medical tape does not compromise the tracking performance of MagDot.

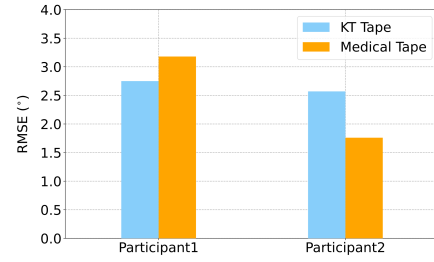


Fig. 20. MagDot with different tapes.

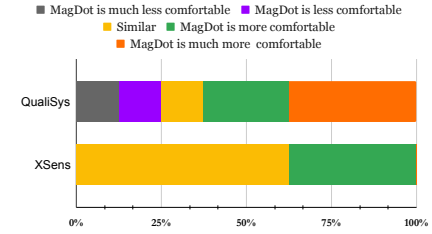


Fig. 22. Comparison of the comfortableness

## 7 USER STUDY OF MAGDOT

Now we analyze the comfortableness of MagDot by conducting a user study among testing subjects. Each participant has experienced the usage of MagDot, QualiSys, and XSens as we elaborated in Sec. 6. We employed a Likert scale metric to differentiate their responses on the level of comfortableness. First, we asked participants about MagDot’s overall comfortableness. Next, we asked four targeted questions regarding participants’ experiences with MagDot. Specifically, these four questions are: (1) Do you feel tight when wearing MagDot? Here, “strongly disagree” and “strongly agree” denote loose and tight fits. (2) Do you agree that putting on MagDot is easy? (3) Do you agree that your joint is highly movable after putting on MagDot? and (4) Do you agree that MagDot has a very compact size? As shown in Fig. 21, 87.5% of participants expressed that MagDot offers a neutral or slightly tight fit. All participants affirmed the wearability of MagDot and the freedom of joint movement is not undermined. Note that all subjects agreed MagDot has a compact form factor.

Next, we asked subjects to compare MagDot’s level of comfortableness with Optic-based (i.e., QualiSys) and IMU-based (i.e., XSens) methods. Participants need to use the Likert scale metric to record their feedback. Next, they were instructed to justify their assessment by answering in text. As shown in Fig. 22, compared with QualiSys system, most participants (62.5%) agreed MagDot outperforms QualiSys in the level of comfortableness. Specifically, they complained that putting on the reflective markers of QualiSys requires extensive assistance (usually more than half an hour) from a Mocap specialist. This tedious process severely undermines their experience of the comfortableness of the QualiSys system. Despite the cost and time-consuming installation process, two subjects mentioned that the reflective markers are more lightweight than both XSens and MagDot, thus facilitating their movements. When comparing with XSens units, participants praised the wearability of XSens units. All participants affirmed that MagDot offers a similar (62.5%) or superior (37.5%) level of comfortableness when compared with XSens.

## 8 RELATED WORKS

### 8.1 Wearable Approaches

**8.1.1 IMU-based Approaches.** Recent works have been focusing on tracking joint angles using IMUs [24, 26–28]. However, existing methods suffer from the acceleration and magnetic interferences mentioned earlier (Sec.2.2), which limits their accuracy in real-world applications. Zhou *et al.* [70] introduced an IMU-based finger motion tracking system with an accuracy of  $9.07^\circ$ . However, this system is excluded for tracking fingers. Recently, progress has been made in reconstructing human poses using sparse worn IMUs, such as the six-IMU setup in [30, 58, 68]. However, these systems can only provide an approximate estimate of the joints’ current states. Liu *et al.* [37] proposed an enhanced approach IMU-based sign language recognition. However, it is not designed for real-time tracking. Liu *et al.* [35] employed a deep learning technique for enhancing the sensing accuracy of the location and orientation of smartwatches. However, this approach is designed exclusively for wrist-worn smartwatches. The demonstrated tracking accuracy may not be sufficient for high-accuracy joint tracking. Wittmann *et al.* [66] proposed a magnetometer-assisted calibration framework for IMU tracking. However, this approach requires the user to perform a predetermined pose for calibration frequently.

**8.1.2 Magnetic sensing.** Compared with IMU-based methods, magnetic sensing approaches are immune to accumulative error, which makes them attractive for joint angle tracking. Previous works on magnetic-based joint angle tracking have typically required placing the sensing unit and corresponding magnet on both sides of the joint [48, 62]. However, accurately measuring the distance between the sensing unit, magnet, and joint is a tedious and error-prone process, which can harm the usability of this approach. In contrast, MagDot’s sensing units can

be attached on both sides of a joint without stringent placement requirements, making it a more practical option for joint angle tracking.

*8.1.3 Flex sensor.* Recently, flex sensors have been explored as an alternative method for monitoring joint motions [23, 29, 36]. By attaching flex sensors to joints, the variation of electrical properties, such as resistance or capacitance, can be proportional to the sensor's bend. For instance, Liu *et al.* [36] utilized the varying resistance of conductive fiber to estimate the elbow angle. Huang *et al.* [29] leveraged the capacitance change of a dielectric elastomer sensor (DES) to observe wrist joint motions. However, this method suffers from poor accuracy in joint tracking. This approach is also susceptible to sensor displacement and stress relaxation issues [29, 36] after repeated use. Recently, Chen *et al.* [23] leveraged capacitive stretchable sensors and learning-based methodologies, e.g., LSTM model as well as transfer learning, to resolve aforementioned issues. However, this approach *only* covered the elbow joint with limited accuracy (average tracking error of  $9.82^\circ$ ). In contrast, MagDot can track elbow, knee, shoulder, and wrist joints with high accuracy.

## 8.2 Unattached Approaches

*8.2.1 Camera-based method.* Motion capture (mocap) method, have long been considered the "gold standard" in fields such as film, gaming, and medicine. Mature commercial systems like Vicon, Qualisys, and Optitrack can track the 3D position of human joints with sub-millimeter accuracy using multiple high-definition cameras and reflective markers. However, mocap systems have very demanding requirements, including extremely high costs and dedicated resources, e.g., equipment and a spacious testing area, making them infeasible for daily use.

Another approach to tracking human body joints is through standalone camera systems, such as the Microsoft Azure Kinect [8], which uses a time-of-flight (ToF) camera. This method offers a non-invasive and relatively low-cost option for joint tracking. However, the accuracy is also susceptible to line-of-sight restrictions.

*8.2.2 Electric magnets.* Existing works also investigated electromagnetic tracking methods. Finexus [22] used a magnetometer array to track the location of electromagnets. Recent methods also leveraged magnetic induction to track electromagnets. For example, [33] leveraged an electromagnetic transponder to track the trajectory of a 3-axis coil, thus facilitating occlusion-free tracking in VR. In AuraRing [46], the authors proposed a wrist-worn coil design that can sense the electromagnetic ring on the user's finger. Aura [64] proposed a head-mounted coil form factor. This approach can be integrated with VR goggles, thus helping sense the position of the electromagnetic coil that resides in the hand-held controller. However, electromagnetic methods are ill-fitted for joint tracking applications. According to Ampere's law, electromagnetic coils usually need several wraps and a high current level to generate a sufficient magnetic field. These requirements usually lead to a bulky form factor and heating problem. In contrast, MagDot leverages passive magnets and magnetometer arrays to achieve a compact and wearable form factor. Our empirical tests demonstrate MagDot is practical for high-accuracy, continuous joint tracking applications.

*8.2.3 RF-based method.* Recent researches have explored the use of radio frequency (RF) technology, including WiFi [32, 59], RFID [67], mmWave [52], and frequency-modulated continuous wave (FMCW) radar [69], for estimating human pose. These methods use RF signals to construct a confidence map and estimate the positions of human joints or body parts to recover posture. While these methods address vision-based problems like occlusion and privacy issues, RF signals can be easily disturbed by interferences such as multipath fading, limiting their accuracy and practicality. Furthermore, dedicated hardware and the high cost of FMCW and RFID systems hinder the deployment of this approach.

## 9 DISCUSSION

As we elaborate in the paper, for joint angle tracking applications, one would need two MagDot units per joint. Compared to the popular IMU-based approach, MagDot does not require more sensor units. Note that for tracking two joint angles, e.g., elbow and shoulder, IMUs may need three sensors. Specifically, the forearm, upper arm, and back. MagDot requires four sensing nodes for achieving two-joint tracking. This is because magnetic sensing requires a shorter sensing range than the IMU-based method. However, the compact size of MagDot can help mitigate the overhead of more sensing nodes.

As we indicated in Sec. 4.2, the cost of each MagDot sensor is only \$35. Compared with the vision-based approach, e.g., VICON and QualiSys, MagDot has a much lower cost. MagDot also offers a more affordable solution compared with high-accuracy IMU units, e.g., XSens. This is because high-accuracy IMU providers usually build their own proprietary systems, including chip design, sensor fusion algorithm, and peripheral interface architecture [3, 5]. In contrast to motion-tracking IMUs, MagDot leverages a novel magnetic sensing framework and COTS magnetometers, making it an affordable, drift-free solution for tracking body movements.

## 10 CONCLUSION

We present MagDot, a wearable joint tracking system that utilizes magnetic sensing for accurate and robust joint angle tracking. Unlike traditional joint tracking methods that rely on optical or inertial sensing, MagDot incorporates a magnet into the sensing platform to improve tracking accuracy and robustness. Our experimental results demonstrate that MagDot can achieve high tracking accuracy for different types of joints. With its superior tracking performance, we believe MagDot holds great potential for a wide range of real-world applications.

## ACKNOWLEDGMENTS

We thank the anonymous reviewers for their suggestions. We also thank students for participating in the experiment, including Jake Wang, Zhenyu Chen, Jiayang Chen, Haoyuan Zeng, and Shanmu Wang. This work was supported by the National Natural Science Foundation of China under Grant No. 62102256. Dongyao Chen is the corresponding author.

## REFERENCES

- [1] 2018. LIS2MDL magnetometer datasheet - production data. <https://www.st.com/resource/en/datasheet/lis2mdl.pdf>. (2018).
- [2] 2018. RAYTAC.MDBT42Q-512KV2. [https://www.raytac.com/product/ins.php?index\\_id=31](https://www.raytac.com/product/ins.php?index_id=31). (2018).
- [3] 2019. MTi 1-series Datasheet. <https://www.xsens.com/hubfs/Downloads/Manuals/MTi-1-series-datasheet.pdf>. (2019).
- [4] 2020. Xsens Magnetic Calibration Manual. [https://www.xsens.com/hubfs/Downloads/Manuals/MT\\_Magnetic\\_Calibration\\_Manual.pdf](https://www.xsens.com/hubfs/Downloads/Manuals/MT_Magnetic_Calibration_Manual.pdf). (2020).
- [5] 2022. User manual of XSens Dot. <https://www.xsens.com/hubfs/Downloads/Manuals/Xsens%20DOT%20User%20Manual.pdf>. (2022).
- [6] 2023a. Datasheet for MLX90393. <https://media.melexis.com/-/media/files/documents/datasheets/mlx90393-datasheet-melexis.pdf>. (2023).
- [7] 2023. KT Tape. <https://www.kttape.com/products/kt-tape-original-cotton>. (2023).
- [8] 2023. Microsoft Azure Kinect. <https://azure.microsoft.com/en-us/products/kinect-dk>. (2023).
- [9] 2023b. MLX90393 Temperature Compensation. <https://www.melexis.com/en/documents/documentation/application-notes/application-note-mlx90393-temperature-compensation>. (2023).
- [10] 2023. NDFEB magnet Technical Data Sheet. [https://www.eclipsemagnetics.com/site/assets/files/22177/eclipsemagnetics\\_ndfeb\\_datasheet.pdf](https://www.eclipsemagnetics.com/site/assets/files/22177/eclipsemagnetics_ndfeb_datasheet.pdf). (2023).
- [11] 2023. QualiSys. <https://www.qualisys.com/>. (2023).
- [12] 2023. QualiSys Arqus A12 camera Tech Specs. <https://www.qualisys.com/cameras/arqus/#!/#tech-specs>. (2023).
- [13] 2023. QualiSys Marker Set. [https://docs.qualisys.com/getting-started/content/10\\_how\\_to\\_prepare\\_your\\_subject/marker\\_sets.htm](https://docs.qualisys.com/getting-started/content/10_how_to_prepare_your_subject/marker_sets.htm). (2023).
- [14] 2023. Vicon. <https://www.vicon.com/>. (2023).
- [15] 2023. Visual 3D, Biomechanics Research Tools. <https://c-motion.com/>. (2023).
- [16] 2023. XSens Motion Capture System. <https://www.movella.com/products/motion-capture>. (2023).



- [17] MD Akhtaruzzaman, Amir Akramin Shafie, and Md Raisuddin Khan. 2016. Gait analysis: Systems, technologies, and importance. *Journal of Mechanics in Medicine and Biology* 16, 07 (2016), 1630003.
- [18] Robert S Behnke and Jennifer Plant. 2021. *Kinetic anatomy*. Human Kinetics.
- [19] Antonio Padilha Lanari Bo, Mitsuhiro Hayashibe, and Philippe Poignet. 2011. Joint angle estimation in rehabilitation with inertial sensors and its integration with Kinect. In *2011 Annual International Conference of the IEEE Engineering in Medicine and Biology Society*. IEEE, 3479–3483.
- [20] Julien Chapleau, Fanny Canet, Yvan Petit, G-Yves Laflamme, and Dominique M Rouleau. 2011. Validity of goniometric elbow measurements: comparative study with a radiographic method. *Clin. Orthop. Relat. Res.* 469, 11 (Nov. 2011), 3134–3140.
- [21] Dongyao Chen, Mingke Wang, Chenxi He, Qing Luo, Yasha Iravantchi, Alanson Sample, Kang G Shin, and Xinbing Wang. 2021. MagX: Wearable, untethered hands tracking with passive magnets. In *Proceedings of the 27th Annual International Conference on Mobile Computing and Networking*. 269–282.
- [22] Ke-Yu Chen, Shwetak N. Patel, and Sean Keller. 2016. Finexus: Tracking Precise Motions of Multiple Fingertips Using Magnetic Sensing. In *Proceedings of the 2016 CHI Conference on Human Factors in Computing Systems*. Association for Computing Machinery, New York, NY, USA, 1504–1514. <https://doi.org/10.1145/2858036.2858125>
- [23] Xiaowei Chen, Xiao Jiang, Jiawei Fang, Shihui Guo, Juncong Lin, Minghong Liao, Guoliang Luo, and Hongbo Fu. 2023. DisPad: Flexible On-Body Displacement of Fabric Sensors for Robust Joint-Motion Tracking. *Proc. ACM Interact. Mob. Wearable Ubiquitous Technol.* 7, 1, Article 5 (mar 2023), 27 pages. DOI: <http://dx.doi.org/10.1145/3580832>
- [24] Glen Cooper, Ian Sheret, Louise McMillian, Konstantinos Silverdis, Ning Sha, Diana Hodgins, Laurence Kenney, and David Howard. 2009. Inertial sensor-based knee flexion/extension angle estimation. *Journal of biomechanics* 42, 16 (2009), 2678–2685.
- [25] Jianjun Cui, Shih-Ching Yeh, and Si-Huei Lee. 2019. Wearable sensors integrated with virtual reality: a self-guided healthcare system measuring shoulder joint mobility for frozen shoulder. *Journal of Healthcare Engineering* 2019 (2019).
- [26] Andrea Giovanni Cutti, Andrea Giovanardi, Laura Rocchi, Angelo Davalli, and Rinaldo Sacchetti. 2008. Ambulatory measurement of shoulder and elbow kinematics through inertial and magnetic sensors. *Medical & biological engineering & computing* 46 (2008), 169–178.
- [27] Mahmoud El-Gohary and James McNames. 2012. Shoulder and elbow joint angle tracking with inertial sensors. *IEEE Transactions on Biomedical Engineering* 59, 9 (2012), 2635–2641.
- [28] Julien Favre, BM Jolles, Rachid Aissaoui, and K Aminian. 2008. Ambulatory measurement of 3D knee joint angle. *Journal of biomechanics* 41, 5 (2008), 1029–1035.
- [29] Bo Huang, Mingyu Li, Tao Mei, David McCoul, Shihao Qin, Zhanfeng Zhao, and Jianwen Zhao. 2017. Wearable stretch sensors for motion measurement of the wrist joint based on dielectric elastomers. *Sensors* 17, 12 (2017), 2708.
- [30] Yinghao Huang, Manuel Kaufmann, Emre Aksan, Michael J Black, Otmar Hilliges, and Gerard Pons-Moll. 2018. Deep inertial poser: Learning to reconstruct human pose from sparse inertial measurements in real time. *ACM Transactions on Graphics (TOG)* 37, 6 (2018), 1–15.
- [31] Sadaf Hashim Hussain, Boonyapat Limthongkul, and Tatyana R Humphreys. 2013. The biomechanical properties of the skin. *Dermatologic Surgery* 39, 2 (2013), 193–203.
- [32] Wenjun Jiang, Hongfei Xue, Chenglin Miao, Shiyang Wang, Sen Lin, Chong Tian, Srinivasan Murali, Haochen Hu, Zhi Sun, and Lu Su. 2020. Towards 3D human pose construction using WiFi. In *Proceedings of the 26th Annual International Conference on Mobile Computing and Networking*. 1–14.
- [33] Wooyoung Kim, Jihoon Song, and Frank C. Park. 2018. Closed-Form Position and Orientation Estimation for a Three-Axis Electromagnetic Tracking System. *IEEE Transactions on Industrial Electronics* 65, 5 (2018), 4331–4337. DOI: <http://dx.doi.org/10.1109/TIE.2017.2760244>
- [34] Naofumi Kitsunezaki, Eijiro Adachi, Takashi Masuda, and Jun-ichi Mizusawa. 2013. KINECT applications for the physical rehabilitation. In *2013 IEEE International Symposium on Medical Measurements and Applications (MeMeA)*. IEEE, 294–299.
- [35] Miaomiao Liu, Sikai Yang, Wyssanie Chomsin, and Wan Du. 2023. Real-Time Tracking of Smartwatch Orientation and Location by Multitask Learning. In *Proceedings of the 20th ACM Conference on Embedded Networked Sensor Systems (SenSys '22)*. Association for Computing Machinery, New York, NY, USA, 780–781. DOI: <http://dx.doi.org/10.1145/3560905.3568096>
- [36] Ruibo Liu, Qijia Shao, Siqi Wang, Christina Ru, Devin Balkcom, and Xia Zhou. 2019. Reconstructing human joint motion with computational fabrics. *Proceedings of the ACM on Interactive, Mobile, Wearable and Ubiquitous Technologies* 3, 1 (2019), 1–26.
- [37] Yilin Liu, Fengyang Jiang, and Mahanth Gowda. 2020. Finger Gesture Tracking for Interactive Applications: A Pilot Study with Sign Languages. *Proc. ACM Interact. Mob. Wearable Ubiquitous Technol.* 4, 3, Article 112 (sep 2020), 21 pages. DOI: <http://dx.doi.org/10.1145/3414117>
- [38] Sebastian OH Madgwick, Andrew JL Harrison, and Ravi Vaidyanathan. 2011. Estimation of IMU and MARG orientation using a gradient descent algorithm. In *2011 IEEE international conference on rehabilitation robotics*. IEEE, 1–7.
- [39] Robert Mahony, Tarek Hamel, and Jean-Michel Pflimlin. 2008. Nonlinear complementary filters on the special orthogonal group. *IEEE Transactions on automatic control* 53, 5 (2008), 1203–1218.
- [40] Adam Morawiec. 2003. *Orientations and rotations*. Springer.

- [41] Jorge J Moré. 2006. The Levenberg-Marquardt algorithm: implementation and theory. In *Numerical Analysis: Proceedings of the Biennial Conference Held at Dundee, June 28–July 1, 1977*. Springer, 105–116.
- [42] Quentin Mourcou, Anthony Fleury, Bruno Diot, Céline Franco, and Nicolas Vuillerme. 2015. Mobile phone-based joint angle measurement for functional assessment and rehabilitation of proprioception. *BioMed research international* 2015 (2015).
- [43] Y Nishio, F Tohyama, and N Onishi. 2007. The sensor temperature characteristics of a fluxgate magnetometer by a wide-range temperature test for a Mercury exploration satellite. *Measurement Science and Technology* 18, 8 (2007), 2721.
- [44] Eshed Ohn-Bar and Mohan M. Trivedi. 2013. Joint Angles Similarities and HOG2 for Action Recognition. In *Proceedings of the IEEE Conference on Computer Vision and Pattern Recognition (CVPR) Workshops*.
- [45] Hongfeng Pang, Dixiang Chen, Mengchun Pan, Shitu Luo, Qi Zhang, and Feilu Luo. 2012. Nonlinear temperature compensation of fluxgate magnetometers with a least-squares support vector machine. *Measurement Science and Technology* 23, 2 (2012), 025008.
- [46] Farshid Salemi Parizi, Eric Whitmire, and Shwetak Patel. 2020. AuraRing: Precise Electromagnetic Finger Tracking. *Proc. ACM Interact. Mob. Wearable Ubiquitous Technol.* 3, 4, Article 150 (sep 2020), 28 pages. DOI : <http://dx.doi.org/10.1145/3369831>
- [47] Timo Pylvänäinen. 2008. Automatic and adaptive calibration of 3D field sensors. *Applied Mathematical Modelling* 32, 4 (2008), 575–587.
- [48] Feini Qu, Brendan D Stoeckl, Peter M Gebhard, Todd J Hullfish, Josh R Baxter, and Robert L Mauck. 2018. A wearable magnet-based system to assess activity and joint flexion in humans and large animals. *Annals of biomedical engineering* 46 (2018), 2069–2078.
- [49] Farshid Salemi Parizi, Wolf Kienzle, Eric Whitmire, Aakar Gupta, and Hrvoje Benko. 2021. RotoWrist: Continuous Infrared Wrist Angle Tracking using a Wristband. In *Proceedings of the 27th ACM Symposium on Virtual Reality Software and Technology*. 1–11.
- [50] Thomas Seel, Jorg Raisch, and Thomas Schauer. 2014. IMU-based joint angle measurement for gait analysis. *Sensors* 14, 4 (2014), 6891–6909.
- [51] Seth J Seidman, Joshua Guag, Brian Beard, and Zane Arp. 2021. Static magnetic field measurements of smart phones and watches and applicability to triggering magnet modes in implantable pacemakers and implantable cardioverter-defibrillators. *Heart Rhythm* 18, 10 (2021), 1741–1744.
- [52] Arindam Sengupta, Feng Jin, Renyuan Zhang, and Siyang Cao. 2020. mm-Pose: Real-time human skeletal posture estimation using mmWave radars and CNNs. *IEEE Sensors Journal* 20, 17 (2020), 10032–10044.
- [53] Sheng Shen, Mahanth Gowda, and Romit Roy Choudhury. 2018. Closing the gaps in inertial motion tracking. In *Proceedings of the 24th Annual International Conference on Mobile Computing and Networking*. 429–444.
- [54] Wolfgang Teufel, Markus Miezal, Bertram Taetz, Michael Fröhlich, and Gabriele Bleser. 2019. Validity of inertial sensor based 3D joint kinematics of static and dynamic sport and physiotherapy specific movements. *PLoS one* 14, 2 (2019), e0213064.
- [55] Jean G Van Bladel. 2007. *Electromagnetic fields*. Vol. 19. John Wiley & Sons.
- [56] Serge van Sint Jan. 2007. *Color atlas of skeletal landmark definitions E-book: guidelines for reproducible manual and virtual palpations*. Elsevier Health Sciences.
- [57] Rachel V. Vitali and Noel C. Perkins. 2020. Determining anatomical frames via inertial motion capture: A survey of methods. *Journal of Biomechanics* 106 (2020), 109832. DOI : <http://dx.doi.org/https://doi.org/10.1016/j.jbiomech.2020.109832>
- [58] Timo Von Marcard, Bodo Rosenhahn, Michael J Black, and Gerard Pons-Moll. 2017. Sparse inertial poser: Automatic 3d human pose estimation from sparse imus. In *Computer graphics forum*, Vol. 36. Wiley Online Library, 349–360.
- [59] Fei Wang, Sanping Zhou, Stanislav Panev, Jinsong Han, and Dong Huang. 2019. Person-in-WiFi: Fine-grained person perception using WiFi. In *Proceedings of the IEEE/CVF International Conference on Computer Vision*. 5452–5461.
- [60] Mingke Wang, Qing Luo, Yasha Iravantchi, Xiaomeng Chen, Alanson Sample, Kang G Shin, Xiaohua Tian, Xinbing Wang, and Dongyao Chen. 2022. Automatic calibration of magnetic tracking. In *Proceedings of the 28th Annual International Conference on Mobile Computing And Networking*. 391–404.
- [61] Kajiro Watanabe and Masaki Hokari. 2006. Kinematical analysis and measurement of sports form. *IEEE Transactions on Systems, Man, and Cybernetics-Part A: Systems and Humans* 36, 3 (2006), 549–557.
- [62] Amanda Watson, Andrew Lyubovskiy, Kenneth Koltermann, and Gang Zhou. 2021. Magneto: joint angle analysis using an electromagnet-based sensing method. In *Proceedings of the 20th International Conference on Information Processing in Sensor Networks (co-located with CPS-IoT Week 2021)*. 1–14.
- [63] Frank Weichert, Daniel Bachmann, Bartholomäus Rudak, and Denis Fisseler. 2013. Analysis of the Accuracy and Robustness of the Leap Motion Controller. *Sensors* 13, 5 (2013), 6380–6393. DOI : <http://dx.doi.org/10.3390/s130506380>
- [64] Eric Whitmire, Farshid Salemi Parizi, and Shwetak Patel. 2019. Aura: Inside-out Electromagnetic Controller Tracking. In *Proceedings of the 17th Annual International Conference on Mobile Systems, Applications, and Services (MobiSys '19)*. ACM, New York, NY, USA, 300–312. DOI : <http://dx.doi.org/10.1145/3307334.3326090>
- [65] Michael W Whittle. 2014. *Gait analysis: an introduction*. Butterworth-Heinemann.
- [66] Frieder Wittmann, Olivier Lamercy, and Roger Gassert. 2019. Magnetometer-Based Drift Correction During Rest in IMU Arm Motion Tracking. *Sensors (Basel, Switzerland)* 19 (2019). <https://api.semanticscholar.org/CorpusID:83460744>
- [67] Chao Yang, Xuyu Wang, and Shuwen Mao. 2020. RFID-pose: Vision-aided three-dimensional human pose estimation with radio-frequency identification. *IEEE transactions on reliability* 70, 3 (2020), 1218–1231.

- [68] Xinyu Yi, Yuxiao Zhou, and Feng Xu. 2021. Transpose: Real-time 3d human translation and pose estimation with six inertial sensors. *ACM Transactions on Graphics (TOG)* 40, 4 (2021), 1–13.
- [69] Mingmin Zhao, Tianhong Li, Mohammad Abu Alsheikh, Yonglong Tian, Hang Zhao, Antonio Torralba, and Dina Katabi. 2018. Through-wall human pose estimation using radio signals. In *Proceedings of the IEEE Conference on Computer Vision and Pattern Recognition*. 7356–7365.
- [70] Hao Zhou, Taiting Lu, Yilin Liu, Shijia Zhang, and Mahanth Gowda. 2022. Learning on the Rings: Self-Supervised 3D Finger Motion Tracking Using Wearable Sensors. *Proc. ACM Interact. Mob. Wearable Ubiquitous Technol.* 6, 2, Article 90 (jul 2022), 31 pages. DOI: <http://dx.doi.org/10.1145/3534587>
- [71] Pengfei Zhou, Mo Li, and Guobin Shen. 2014. Use it free: Instantly knowing your phone attitude. In *Proceedings of the 20th annual international conference on Mobile computing and networking*. 605–616.